RESEARCH ARTICLE

Key Points:
- VIIRS on-orbit calibration
  methodology
- VIIRS onboard calibrators and sensor
  operation activities
- VIIRS on-orbit performance

Supporting Information:
- Readme
- Supplemental Figures S1–S32 and
  Tables S1–S23

Correspondence to:
X. Xiong,
Xiaoxiong.Xiong-1@nasa.gov

VIIRS on-orbit calibration methodology and performance

Xiaoxiong Xiong[1], James Butler[1], Kwofu Chiang[2], Boryana Efremova[2], Jon Fulbright[2], Ning Lei[2], Jeff McIntire[2], Hassan Oudrari[2], Junqiang Sun[2], Zhipeng Wang[2], and Aisheng Wu[2]

[1]Sciences and Exploration Directorate, NASA/GSFC, Greenbelt, Maryland, USA, [2]Sigma Space Corporation, Lanham, Maryland, USA

Abstract The Visible Infrared Imaging Radiometer Suite (VIIRS) sensor aboard the Suomi National Polar-orbiting Partnership spacecraft has successfully operated since its launch in October 2011. The VIIRS collects data in 22 spectral bands that are calibrated by a set of onboard calibrators (OBC). In addition, lunar observations are made to independently track VIIRS long-term calibration stability for the reflective solar bands (RSB). This paper provides an overview of VIIRS OBC functions as well as its on-orbit operation and calibration activities. It also describes sensor calibration methodologies and demonstrates VIIRS on-orbit performance from launch to present. Results reported in this paper include on-orbit changes in sensor spectral band responses, detector noise characterization, and key calibration parameters. Issues identified and their potential impacts on sensor calibration are also discussed. Since launch, the VIIRS instrument nominal operation temperature has been stable to within ±1.0 K. The cold focal plane temperatures have been well controlled, with variations of less than 20 mK over a period of 1.5 years. In general, changes in thermal emissive bands (TEB) detector responses have been less than 0.5%. Despite large response degradation in several near-infrared and short-wave infrared bands and large SD degradation at short visible wavelengths, the VIIRS sensor and OBC overall performance has been excellent postlaunch. The degradation caused by the telescope mirror coating contamination has been modeled and its impact addressed through the use of modulated relative spectral response in the improved calibration and the current sensor data record data production. Based on current instrument characteristics and performance, it is expected that the VIIRS calibration will continue to meet its design requirements, including RSB detector signal to noise ratio and TEB detector noise equivalent temperature difference, throughout its 7 year design lifetime.

1. Introduction

The Suomi National Polar-orbiting Partnership (S-NPP), formerly known as the National Polar-orbiting Operational Environmental Satellite System Preparatory Project, was developed as (1) the next generation polar-orbiting weather satellite system and (2) the bridge mission to provide a critical linkage between the observations and data records generated from the Earth Observing System (EOS) and the future Joint Polar Satellite System satellites [*Murphy et al.*, 2006]. The Visible Infrared Imaging Radiometer Suite (VIIRS) is one of the key instruments on board the S-NPP satellite launched on 28 October 2011. Designed and built by the same instrument vendor, the VIIRS is a follow-on instrument to the Moderate Resolution Imaging Spectroradiometer (MODIS), currently operated on board the EOS Terra and Aqua satellites [*Barnes et al.*, 2003; *Salomonson et al.*, 2002; *Xiong et al.*, 2008]. VIIRS is a scanning radiometer with a rotating telescope assembly (RTA), making daily global measurements in 22 spectral bands in the visible (VIS), near-infrared (NIR), short-wave infrared (SWIR), midwave infrared (MWIR), and long-wave infrared (LWIR) regions. Key spectral band design requirements are shown in Table 1. The 14 bands in the VIS, NIR, and SWIR are referred to as the reflective solar bands (RSB), while the 7 in the MWIR and LWIR are the thermal emissive bands (TEB). In addition, VIIRS has a panchromatic day/night band (DNB) used for low light detection. S-NPP VIIRS is operated continuously and produces 22 environmental data records (EDRs), which enable a broad range of applications, from environmental and hazard monitoring to numerical weather prediction and long-term climate change monitoring [*Ardanuy et al.*, 2002; *Lee et al.*, 2006; *Schueler et al.*, 2002]. The EDRs are derived from the sensor data records (SDRs), which include calibrated and geolocated reflectance and radiance, as well as brightness temperatures for the MWIR and LWIR spectral bands. To assure sensor on-orbit calibration and data quality, the VIIRS instrument carries a set of onboard calibrators (OBCs), designed and improved based on the

Table 1. VIIRS Spectral Band Design Specifications and On-Orbit Performance (Radiance Unit: W/m^2/μm/sr)

FPA	Band No.	Spectral Range (μm)	Band Gain	Ltyp or Ttyp (K) Spec	Lmax or Tmax	SNR or NEdT (K) Spec	SNR or NEdT/Spec (Prelaunch)	SNR or NEdT/Spec (02/06/2012)	SNR or NEdT/Spec (05/22/2012)	SNR or NEdT/Spec (09/10/2012)	SNR or NEdT/Spec (12/17/2012)	SNR or NEdT/Spec (03/18/2013)
VIS/NIR	M1	0.402–0.422	High	44.9	135	352	1.75	1.69	1.70	1.66	1.70	1.72
			Low	155	615	316	3.46	3.37	3.34	3.32	3.42	3.54
	M2	0.436–0.454	High	40	127	380	1.64	1.54	1.56	1.53	1.57	1.56
			Low	146	687	409	2.73	2.58	2.54	2.53	2.62	2.63
	M3	0.478– 0.498	High	32	107	416	1.66	1.53	1.56	1.54	1.57	1.54
			Low	123	702	414	2.68	2.49	2.50	2.45	2.50	2.54
	M4	0.545–0.565	High	21	78	362	1.61	1.50	1.54	1.49	1.54	1.50
			Low	90	667	315	3.06	2.72	2.83	2.78	2.89	2.77
	I1	0.600–0.680	Single	22	718	119	2.02	1.79	1.77	1.76	1.76	1.76
	M5	0.662–0.682	High	10	59	242	1.51	1.37	1.33	1.35	1.34	1.30
			Low	68	651	360	2.30	1.74	1.68	1.69	1.68	1.65
	M6	0.739–0.754	Single	9.6	41	199	2.09	1.82	1.74	1.74	1.70	1.69
	I2	0.846–0.885	Single	25	349	150	2.03	1.72	1.61	1.55	1.52	1.50
	M7	0.846–0.885	High	6.4	29	215	2.42	2.08	1.97	1.87	1.84	1.80
			Low	33.4	349	340	2.49	1.83	1.68	1.61	1.57	1.53
S/MWR	M8	1.230–1.250	Single	5.4	165	74	3.69	3.10	2.84	2.73	2.65	2.60
	M9	1.371–1.386	Single	6	77.1	83	3.05	2.79	2.64	2.54	2.50	2.47
	I3	1.580–1.640	Single	7.3	72.5	6	28.67	25.48	24.49	24.12	23.75	23.58
	M10	1.580–1.640	Single	7.3	71.2	342	2.09	1.74	1.68	1.68	1.65	1.60
	M11	2.225–2.275	Single	0.12	31.8	10	2.50	2.21	2.21	2.16	2.15	2.14
	I4	3.550–3.930	Single	270 (K)	353	2.5 (K)	0.16	0.16	0.16	0.16	0.16	0.16
	M12	3.610–3.790	Single	270 (K)	353	0.396 (K)	0.33	0.33	0.33	0.33	0.28	0.30
	M13	3.973–4.128	High	300 (K)	343	0.107 (K)	0.37	0.37	0.37	0.37	0.37	0.37
			Low	380 (K)	634	0.423 (K)	N/A	N/A	N/A	N/A	N/A	N/A
LWR	M14	8.400–8.700	Single	270 (K)	336	0.091 (K)	0.66	0.55	0.66	0.66	0.66	0.66
	M15	10.263–11.263	Single	300 (K)	343	0.07 (K)	0.43	0.43	0.43	0.43	0.43	0.43
	I5	10.500–12.400	Single	210 (K)	340	1.5 (K)	0.27	0.27	0.27	0.27	0.27	0.27
	M16	11.538–12.488	Single	300 (K)	340	0.072 (K)	0.56	0.42	0.42	0.42	0.42	0.42

experience and lessons from MODIS, which include a solar diffuser (SD) and a solar diffuser stability monitor (SDSM) primarily used for the RSB calibration and a blackbody (BB) for the TEB. The improvements made in VIIRS OBCs include a modified SDSM design to minimize the nonuniform solar illumination present in the MODIS SDSM Sun view responses and a new SD solar attenuation screen (SAS) design to reduce the earthshine impact on SD calibration. Like MODIS, regularly scheduled lunar observations are also an important element for the VIIRS sensor on-orbit calibration and characterization [*Cao et al.*, 2013; *De Luccia et al.*, 2012a; *Sun et al.*, 2012; *Xiong et al.*, 2007a, 2009, 2010].

Currently, both the instrument and its OBCs are operated normally. Critical calibration parameters are derived routinely and updated frequently into the data production system. A number of improvements have been made to maintain sensor on-orbit calibration and data quality. Section 2 of this paper provides an overview of VIIRS instrument operation and calibration activities with a focus on those related to sensor on-orbit calibration and characterization and the use of its OBCs. Section 3 briefly describes sensor on-orbit calibration methodologies and lunar calibration strategies. In section 4, the results of sensor and OBC on-orbit performance, including changes in spectral band responses and noise characterization, are presented and discussed. Results show that the VIIRS operation has been very stable with well-controlled cold focal plane assembly (CFPA) and BB temperatures. The instrument temperatures, including seasonal variations, for the scan cavity and warm FPA (VIS and NIR) have been stable to within ±1.0 K. The variations of the CFPA and BB temperatures, including their drifts over time, have been of less than 20 mK and 5 mK, respectively. The SD on-orbit degradation has exhibited similar wavelength dependence as MODIS, that is, larger degradation at shorter wavelengths. Both RSB and TEB responses are frequently monitored by the OBCs. In general, the TEB detector responses are extremely stable, but the RSB responses show large changes at NIR and SWIR wavelengths, primarily due to RTA mirror coating contamination [*Iona et al.*, 2012; *De Luccia et al.*, 2012b; *Lei et al.*, 2012a]. Calibration coefficients are derived and updated frequently in support of VIIRS operational calibration and data production. Also discussed in this paper are issues identified, their potential impacts, and mitigation strategies. Despite large response degradation in several NIR and SWIR bands, the VIIRS overall performance will continue to meet the sensor design requirements over its 7 year design lifetime.

2. Sensor Operation and Calibration Activities

The VIIRS sensor consists of two modules (Figure 1): the electronics module providing electronic interfaces between VIIRS and the spacecraft; and the opto-mechanical module containing all the optical and mechanical components that include the OBCs, RTA with a half-angle mirror (HAM), aft optics, and FPAs. The 22 spectral bands include 16 moderate (M) resolution bands with a nadir spatial resolution of 750 m, 5 imaging (I) bands at 375 m nadir spatial resolution, and a day/night band (DNB) at 750 m. The M and I band detectors are located on
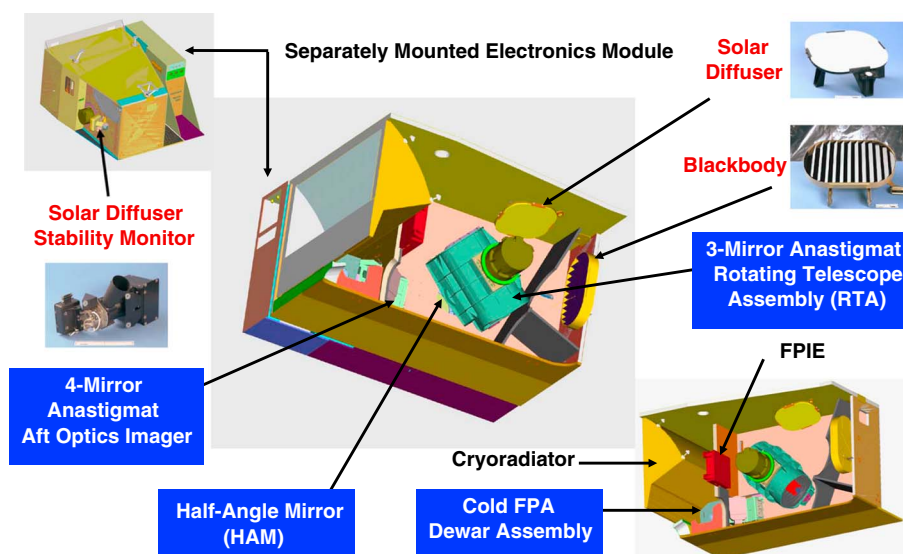

Figure 1. VIIRS sensor and on-board calibrators.

Table 2. Center Wavelengths of VIIRS SDSM Detectors

SDSM Detector	1	2	3	5	5	6	7	8
Wavelength (μm)	0.412	0.445	0.488	0.555	0.672	0.745	0.865	0.926

three focal planes: VIS/NIR, S/MWIR, and LWIR. The DNB has its own FPA adjacent to the VIS/NIR FPA and consists of charge coupled device (CCD) arrays operated in a time-delay-integration mode. Both the S/MWIR and LWIR FPAs are cooled and nominally controlled at 80 K via a passive cryoradiator. Among the moderate resolution bands, M1–M5, M7, and M13 are dual gain bands. Their transitions from high gain (for low radiance) to low gain (for high radiance) or vise versa are performed on board at the focal plane level described in the Sensor Specification for VIIRS by Raytheon Company (unpublished document, 2007).

The HAM is a double-sided rotating mirror. It rotates at half the speed of the RTA, thus each complete revolution or scan of the RTA uses only one side of the HAM and each subsequent scan uses the other side of the HAM. Each scan includes the data collection sequence from the space view (SV), Earth view (EV), BB, and SD views. The SV and EV data sectors are part of the view through the open nadir aperture door. The SV data provides measurements for the instrument background. The temperature-controlled on-board BB is the calibration source for the TEB. It is monitored by six embedded thermistors traceable to National Institute of Standards and Technology and protected by a shield plate from stray light. It has a V-groove design with high emissivity ($\varepsilon > 0.996$). The SD panel, located behind a solar attenuation screen (SAS), is at the instrument front end. It enables the RSB detector gains to be monitored once per orbit. The SD bidirectional distribution function (BRDF) was characterized prelaunch and its on-orbit degradation is monitored by the SDSM. The SDSM is essentially a ratioing radiometer, which consists of an integrating sphere and eight filtered detectors, covering the wavelength range from 0.41 to 0.93 μm (Table 2).

VIIRS went through extensive prelaunch testing at both the sensor and spacecraft levels to mimic sensor responses in the space environment. Shortly after launch, VIIRS successfully carried out a series of instrument tests and characterization activities to verify its space environment operations and various OBC functions as well as to evaluate and verify its on-orbit performance. During the first 6 months of the intensive calibration and validation (ICV) period, three different types of spacecraft maneuvers were performed: (i) roll maneuvers for lunar observations to support RSB calibration, (ii) yaw maneuvers to characterize the SAS and SDSM screen transmission functions combined with the SD BRDF, and (iii) a pitch maneuver to validate the TEB response versus scan angle (RVS). For on-orbit characterization of the SAS and SDSM screen transmissions, 14 yaw maneuvers were executed to acquire data over a large solar angle range within a short time period (15–16 February 2012). Since launch, lunar roll maneuvers have been scheduled regularly [*Butler et al.*, 2012; *Oudrari et al.*, 2012; *Xiong et al.*, 2012]. The timeline of all maneuvers and other major operation events and calibration activities are listed in Table 3.

Table 3. Key Operation and Calibration Events of S-NPP VIIRS

Event #	Date	Event Description
1	10/28/2011	Suomi-NPP launch
2	11/08/2011	VIIRS turned on
3	11/21/2011	Nadir door open
4	01/04/2012	First lunar calibration (roll maneuver)
5	01/18/2012	Cryo-cooler door open
6	02/03/2012	Second lunar calibration (roll maneuver two orbits)
7	02/06/2012	First OBC blackbody warm-up cool-down
8	02/15/2012	Yaw maneuver (one time event)
9	02/20/2012	Pitch maneuver (one time event)
10	03/03/2012	Third lunar calibration (roll maneuver)
11	04/02/2012	Fourth lunar calibration (roll maneuver)
12	05/02/2012	Fifth lunar calibration (roll maneuver)
13	05/22/2012	Second OBC blackbody warm-up cool-down
14	05/31/2012	Sixth lunar calibration (no maneuver)
15	09/10/2012	Third OBC blackbody warm-up cool-down
16	10/25/2012	Seventh lunar calibration (roll maneuver)
17	11/23/2012	Eighth lunar calibration (roll maneuver)
18	12/17/2012	Fourth OBC blackbody warm-up cool-down
19	12/23/2012	Ninth lunar calibration (roll maneuver)
20	01/22/2013	Tenth lunar calibration (roll maneuver)
21	02/21/2013	Eleventh lunar calibration (roll maneuver)
22	03/18/2013	Fifth OBC blackbody warm-up cool-down
23	03/23/2013	Twelfth lunar calibration (roll maneuver)
24	04/21/2013	Thirteenth lunar calibration (roll maneuver)
25	05/21/2013	Fourteenth lunar calibration (no maneuver)

With the exception of when the RTA was stowed very briefly during ICV, the on-board SD calibration data has been collected once per orbit since the VIIRS "Turn On" on 8 November 2011. Initially, the SDSM was operated every orbit to monitor SD on-orbit degradation. Since 28 February 2012, the SDSM calibration frequency has been reduced to once daily. The on-board BB is nominally controlled at 292.5 K. Once every 3 months, a BB warm-up and cool-down (WUCD) operation is performed. The WUCD data sets, collected over a wide range of BB temperatures, help characterize BB performance, track the TEB detector noise equivalent temperature difference (NEdT), and monitor detector response nonlinearity. As of 31 May 2013, five WUCD operations have been successfully performed.

For RSB calibration stability monitoring, VIIRS lunar observations are made with the lunar phase angles limited to a small range, currently from −51.5° to −50.5°, where the negative (positive) phase angle is used for a waxing (waning) Moon. Due to spacecraft operational constraints, lunar observations are made through the instrument SV, with the roll angles kept from −14° to −1°. In order to capture lunar images for all spectral bands at the same time, a sector rotation is implemented such that the EV data sector is centered on the SV. The dual gain bands are set to fixed high gain during scheduled lunar observations [*Sun et al.*, 2012].

3. On-Orbit Calibration Methodologies

The VIIRS EV (path) radiance is retrieved using a quadratic calibration algorithm from its background-subtracted detector response (dn_{EV}),

$$L_{EV} = F \cdot (c_0 + c_1 \cdot dn_{EV} + c_2 \cdot dn_{EV^2}) / RVS_{EV} \qquad (1)$$

where c_0, c_1, and c_2 are instrument temperature dependent prelaunch calibration coefficients, RVS_{EV} is detector's response versus scan angle at the EV viewing angle, and F is an on-orbit calibration scaling factor. The value of F is determined by the ratio of known calibration source spectral radiance (L_{CS}) to the retrieved source spectral radiance (L_{RET}),

$$F = L_{CS} / L_{RET} \qquad (2)$$

where

$$L_{RET} = (c_0 + c_1 \cdot dn_{CS} + c_2 \cdot dn_{CS}^2) / RVS_{CS}. \qquad (3)$$

The dn_{CS} and RVS_{CS} in equation (3) are the detector response to the calibration source and the RVS at the calibration source view angle, respectively. The computation of L_{CS} depends on TEB and RSB and their calibration sources.

3.1. Reflective Solar Bands Calibration

VIIRS RSB calibration is referenced to the onboard SD BRDF. When fully illuminated by the Sun through an attenuation screen, the SD provides a known calibration source spectral radiance (L_{SD}). It is used together with the retrieved spectral radiance (L_{RET}) from SD on-orbit observations, available each orbit, to derive the F factor (i.e., L_{SD}/L_{RET}) for the RSB calibration. The L_{RET} is computed using equation (3) with the subscript CS replaced by SD. The calibration source spectral radiance from the SD (L_{SD}) is proportional to the solar spectral irradiance (E_{SUN}), SD SAS transmission function (τ_{SAS}), SD BRDF, and weighted by the detector's relative spectral response (RSR),

$$L_{SD} = [\tau_{SAS} \cdot \cos(\theta_{SD}) / d^2] \cdot \int [RSR(\lambda) \cdot E_{SUN}(\lambda) \cdot BRDF(\lambda) \cdot d\lambda] / \int [RSR(\lambda) \cdot d\lambda] \qquad (4)$$

where θ_{SD} is the SD solar zenith angle and d the distance (normalized to 1 AU) between the Sun and sensor. It should be pointed out that the F factor is computed scan-by-scan using SD calibration data when it is fully illuminated by the Sun, and is band, detector, and HAM side dependent [*Lei et al.*, 2012a].

The F factor determination utilizing the SD views requires constant monitoring of the SD BRDF, which degrades with exposure to UV light. The greatest degradation is at shorter wavelengths and the degradation is minimal at wavelengths longer than about 0.90 μm [*Bruegge et al.*, 1993; *Xiong et al.*, 2007b, 2010]. The degradation of the SD BRDF is quantified as the H factor, which is wavelength and time dependent and can be expressed as

$$H(\lambda, t) = BRDF(\lambda, t) / BRDF_0(\lambda) \qquad (5)$$

where $BRDF(\lambda, t)$ and $BRDF_0(\lambda)$ are the SD on-orbit BRDF at time t and its initial prelaunch BRDF, respectively. The H factor is calculated for the RSB bands with wavelengths shorter than 0.93 μm. Since the SD degradation

at wavelengths above 1.0 μm is extremely small, the H factor is set to 1.0 for the RSB SWIR bands [*Xiong et al.*, 2007c].

The SDSM is a ratioing radiometer with eight detectors covering wavelengths from 0.41 to 0.93 μm (Table 2). It measures the change in SD BRDF over time and operates while the Sun illuminates the SD panel. The SDSM compares the response from the illuminated SD (through the SAS) to a direct view of the Sun through a separate attenuation screen. The H factor is effectively the ratio of the SDSM's SD view response (dc_{SD}) to its Sun view response (dc_{SUN}),

$$H(\lambda, t) \propto [dc_{SD}/(\tau_{SAS} \cdot \cos(\theta_{SD}))]/[dc_{SUN}/\tau_{SUN}] \tag{6}$$

where τ_{SAS} and τ_{SUN} are the SD SAS transmission and the SDSM Sun view screen transmission, respectively. The design is very similar to the MODIS SDSM [*Xiong et al.*, 2007c]. A full description of the data analysis can be found in the VIIRS Radiometric Calibration Algorithm Theoretical Basis Document ATBD by S. Mills (unpublished document, 2010) available from the U.S. NOAA Center for Satellite Applications and Research (http://www.star.nesdis.noaa.gov/). It should be noted that the SDSM tracks SD degradation at a different angle than that viewed by the sensor. The SDSM design and function assume SD degradation is the same at both angles. This assumption is reasonable considering the fact that the SD panel is made of space-grade Spectralon with a near-Lambertian surface.

Like the SD, the Moon can also be used as a calibration target. The lunar irradiance observed by the sensor strongly depends on the viewing geometry (e.g., phase angle) and can be computed from detectors' responses to the Moon. Together with lunar irradiance predicated by the United States Geological Survey Robotic Observatory Lunar Observatory model, a band-averaged lunar F factor can be derived [*Kieffer and Stone*, 2005; *Sun et al.*, 2012]. In general, the relative uncertainty of model predicted lunar irradiance is approximately 1% among different lunar viewing geometries. By limiting lunar phase angles to a small range, the relative uncertainty of the lunar model irradiance could be much smaller than 1%. Currently, the four middle scans from each lunar observation, each viewing the whole Moon, are used to compute the integrated lunar irradiance for each spectral band.

3.2. Thermal Emissive Bands Calibration

The VIIRS TEB calibration is performed using its on-board BB. The TEB F factor is derived from the calibration source spectral radiance (L_{CS}), which includes contributions from the BB, RTA, and HAM,

$$L_{CS} = L_{BB} + (1 - RVS_{SV}/RVS_{BB}) \cdot [(1 - \rho_{RTA}) \cdot L_{RTA} - L_{HAM}]/\rho_{RTA} \tag{7}$$

where L_{BB}, L_{RTA}, and L_{HAM} are the radiances of the BB, RTA, and HAM averaged over the detector RSR, RVS_{SV} and RVS_{BB} are the RVS at SV and BB scan angles respectively, and ρ_{RTA} is the reflectivity of the RTA. The retrieved spectral radiance (L_{RET}) is computed from BB observations using equation (3) with the subscript CS replaced by BB. The BB radiance includes its thermal emission and the surrounding thermal emissions reflected from the BB surface. The BB thermal emission is the dominant term for the TEB calibration source spectral radiance, as the surface reflected thermal emission is generally very small. Other small contributions from the RTA and HAM shown in equation (7) are mainly due to the RVS difference between the BB and SV. Similar small contributions also need to be considered for the EV path radiance term in equation (1) for the TEB calibration. The BB is nominally set at 292.5 K and its WUCD is performed once every 3 months. During BB WUCD operations, the BB temperature varies from instrument ambient to 315 K, enabling the detector's offset and nonlinear response to be characterized. The TEB F factor is computed scan-by-scan. A full description of the TEB calibration can also be found in the VIIRS ATBD by S. Mills (unpublished document, 2010).

3.3. Special Topics

The SD SAS transmission function (τ_{SAS}) and SD BRDF are key parameters used to compute RSB on-orbit calibration coefficients. These parameters (functions) were characterized prelaunch typically with limited illumination and viewing angles and at a number of selected wavelengths. Based on lessons learned from MODIS, data collected from a series of carefully scheduled yaw maneuvers can be used to characterize the SD BRDF and its screen transmission function [*Xie et al.*, 2005; *Xiong et al.*, 2007b]. For VIIRS, the RSB F factor equation can be inverted to solve for the product of the SD BRDF and SAS transmission at the RTA view. An iterative process is performed in which prelaunch measurements of the transmission factors are used to derive the on-orbit transmission factors from yaw maneuver data. Iterations continue until convergence
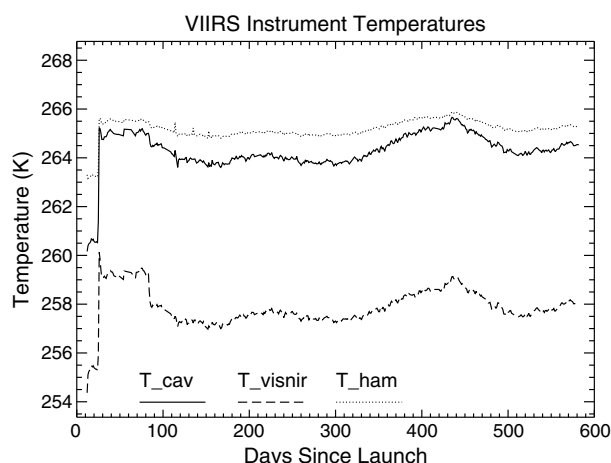
Figure 2. VIIRS instrument cavity, VIS/NIR FPA, and HAM temperatures (daily averaged).

occurs. Similarly, the *H* factor equation is inverted to solve for the product of the SD BRDF and SAS transmission at the SDSM SD view from the yaw maneuver data. Next, the derived SD BRDF and SAS transmission product (SDSM SD view) is used to determine the SDSM solar screen transmission from the *H* factor equation. This process is iterated until convergence and both transmission factors are normalized to their highest value [*McIntire et al.*, 2012].

The VIIRS pitch maneuver was performed on 20 February 2012 and data collected during the pitch maneuver were used to characterize and validate the TEB RVS. When the sensor views deep space (i.e., an extremely cold target), the only radiance contributions are the thermal emissions from the RTA and HAM, which are proportional to the RVS difference between the EV and SV. As a result, the TEB relative RVS_{EV} can be derived from TEB detector's EV response to the deep space [*Wu et al.*, 2012]. In this process, the sensor's view to the BB continues to provide critical calibration information. Similar to prelaunch, a second order polynomial is used to fit the RVS as a function of angle of incidence (AOI) on the HAM.

Shortly after launch, large response degradation was observed in several NIR and SWIR bands, which was caused by the RTA mirror coating contamination [*Barrie et al.*, 2012; *Iona et al.*, 2012]. Because of this, methodologies have been developed to model the response degradation and to predict sensor performance at the end of its design lifetime. Details of the degradation model and related data analyses have been reported elsewhere [*Lei et al.*, 2012b]. To mitigate the calibration impact due to wavelength dependent response degradation, a modulated RSR has been derived and applied in the RSB calibration.

4. Results and Discussion

Excluding special calibration and characterization events at the beginning of mission, VIIRS on-orbit operation has been extremely stable. Figure 2 illustrates VIIRS instrument cavity, VIS/NIR FPA, and HAM temperatures. There is no temperature control for the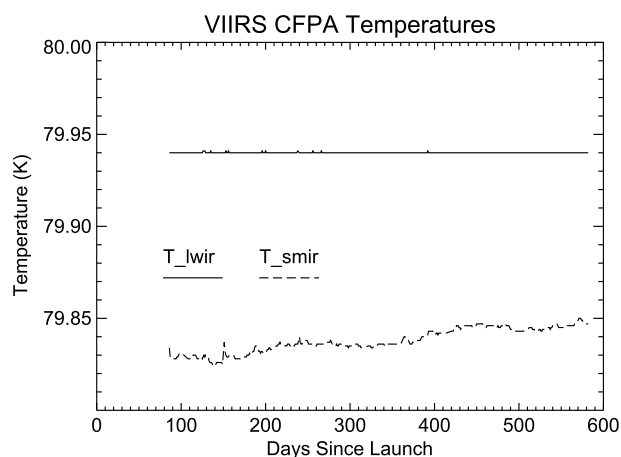 VIS/NIR FPA. As a result, it follows closely with the instrument cavity temperature. Except at the beginning of instrument turn-on and the small, but expected, seasonal variations on the order of ±1.0 K, the overall instrument temperatures have been very stable. Meanwhile, the S/MWIR and LWIR FPAs are nominally controlled at 80 K and their stability, better than 20 mK from launch to present, is demonstrated in Figure 3. The trending begins at day 86 after launch (21 January 2012) when the cold FPA temperatures stabilized shortly after opening the cooler door. Presented in Figure 4 is the onboard BB temperature trending averaged over six thermistors. Small time periods of BB WUCD, spacecraft anomaly, and instrument safe mode are excluded from this
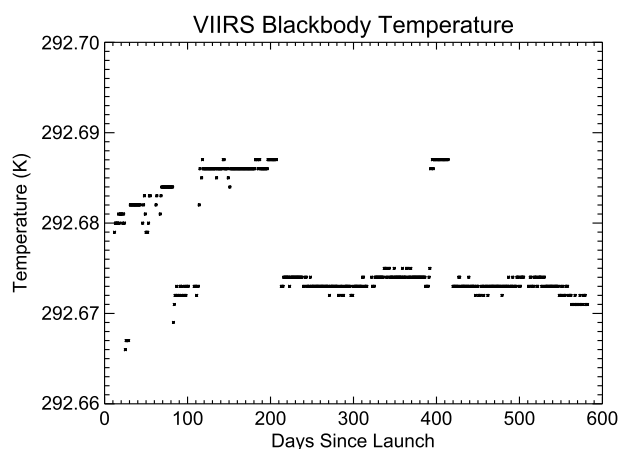

Figure 3. VIIRS S/MWIR and LWIR FPA temperatures (daily averaged). The trending starts from day 86 (21 January 2012) when the CFPA temperatures stabilized after opening the cooler door.

Figure 4. VIIRS BB temperature trending (daily averaged over all six BB thermistors).

trending. There is a small distinct offset of about 15 mK in the BB temperature trending. This is due to the use of two different blackbody default settings at the end of WUCD and following an instrument reset. It is clear that the BB temperature is controlled with excellent stability at its nominal operational settings and typical variations are less than 5 mK.

The SDSM system on VIIRS has tracked the SD on-orbit degradation well. Currently, the *H* factors are computed using equation (6) with on-orbit updated SD and SDSM screen transmission derived from the yaw maneuvers. Figure 5 displays the eight *H* factors over the lifetime of the mission with normalization made to the first on-orbit SDSM calibration. The bluest band (detector 1) indicates that the SD has degraded by more than over 20% since launch, yet the degradation is less than 1% at wavelengths above 0.865 μm. There are a few undulations in the *H* factor trends, and these are most likely due to unresolved features in the transmission functions of the attenuation screens derived from the yaw maneuver data. In order to continuously and accurately track SD on-orbit degradation, other small effects need to be carefully monitored and addressed if necessary. It was discovered postlaunch that the filters used on the SDSM detectors may have out-of-band (OOB) response. Fortunately, the calibration impact due to the filter OOB response is believed to be negligible for all but the three bluest bands, M1, M2, and M3. A comprehensive impact assessment due to SDSM detector OOB response on these three bands is ongoing. It should be possible to evaluate the effect of the OOB response on the *H* factors for these bands by comparing the *F* factors derived by the SD method and those derived by the lunar method.

The normalized RSB 1/*F* factors (or gains) derived from SD calibration are shown in Figure 6a for bands I1, I2, and M4–M7, Figure 6b for bands M1–M3, and Figure 6c for bands M8–M11 and I3 (the solid lines). The normalization is made to the value on the first available date: 8 November 2011 for VIS/NIR bands and 21 January 2012 for SWIR bands (M8–M11 and I3). The 1/*F* factors shown in Figure 6 are daily averaged values over all detectors and HAM sides for each spectral band. No additional fitting or smoothing is made in Figure 6. It should be noted that the product of SD BRDF and SAS transmis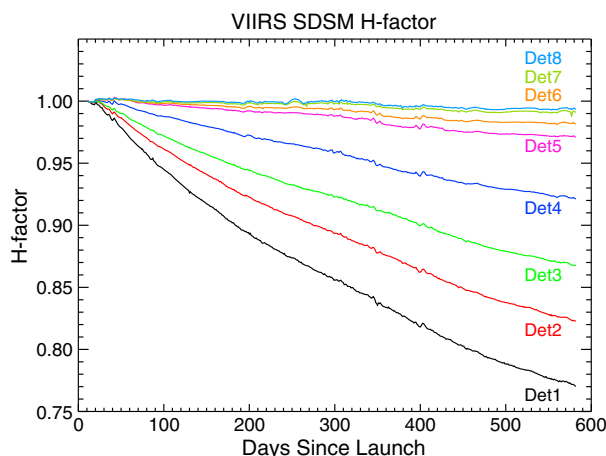sion derived from the yaw data is currently used to calculate the *F* factors for each spectral band. A noticeable feature in Figure 6 is the quick decrease in the 1/*F* factors for NIR and SWIR bands. For the I2 and M7 bands, the 1/*F* factors have decreased about 32%. The root cause of this quick decrease in the 1/*F* factors is RTA mirror contamination by tungsten oxides which become light absorbent when exposed to UV light [*Iona et al.*, 2012; *De Luccia et al.*, 2012b; *Barrie et al.*, 2012]. The optical throughput decrease due to mirror contamination has slowed significantly over time. Despite the decrease of some RSB throughput due to RTA radiometric degradation, the projected signal to noise ratio for each RSB band
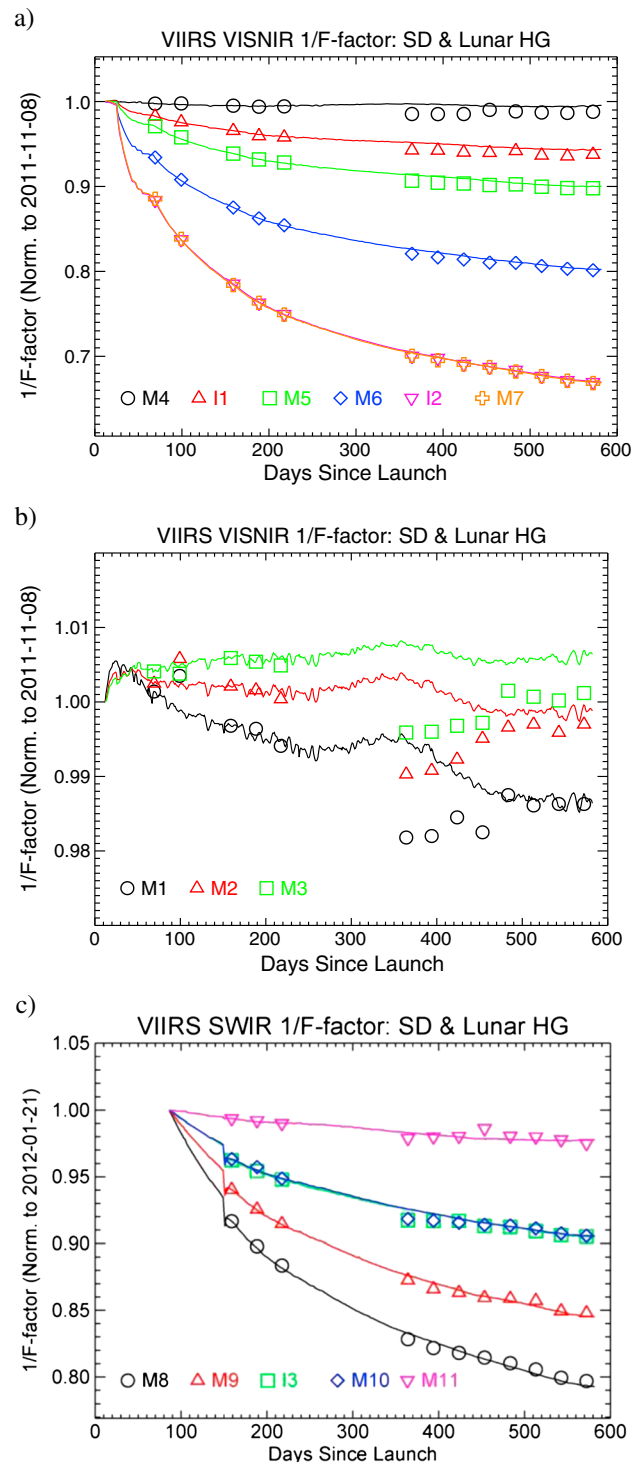

Figure 5. SDSM detectors *H* factor trending. The eight *H* factors are plotted over the lifetime of the mission.

a)

b)

c)

Figure 6. RSB detectors gain (1/*F*) trending from the solar diffuser (lines) and lunar calibration (symbols). Band averaged *F* factors are computed by the daily average of all detectors and both HAM sides. (a) VIS/NIR bands I1, I2, M4–M7; (b) VIS/NIR bands M1–M3; and (c) SWIR bands M8–M11, I3.

will continue to meet the design requirements at the end of 7 years of operation. Another feature can be seen near day 140 (since launch) when the SWIR band 1/*F* factors dipped out-of-trend. Right before the dip, the spacecraft was briefly in Sun Point mode, resulting in the spacecraft control computer reset likely due to overheating. The root cause for the dip remains to be understood.

As described in section 4, relative *F* factors for the RSB can be derived from regularly scheduled lunar observations. For comparison purposes, the lunar results are also presented as symbols in Figure 6. The lunar 1/*F* factors (gains) are normalized to the SD gains at the April 2012 lunar observation for each spectral band. It is clear that the 1/*F* factors from both calibration approaches agree well for most spectral bands. The largest difference, about 1%, occurs in band M1. For other bands, the differences are less than 0.5%. Among these, band M7 (0.865 μm) has degraded most while band M1 (0.412 μm) has the least degradation. VIIRS RSB degradation behavior is different from MODIS RSB where the larger degradation occurs at the shorter wavelength bands [*Sun et al.*, 2007; *Xiong et al.*, 2007b, 2010].

The band-averaged 1/*F* factor trend of the TEB bands (HAM side A) since 20 January 2012 when the cold FPAs reached their nominal temperatures is shown in Figure 7. Every point represents a daily averaged *F* factor over all valid scans in all granules near the passage of the spacecraft over the South Pole. The discontinuities in the *F* factor trend are coincident with spacecraft maneuvers and anomalies during which the cold FPA temperatures changed. The 1/*F* factor trend since the SC anomaly on 24 March 2012 is stable with I5 and M12 showing the most noticeable trends

with values of 0.44% and 0.30%, respectively. Generally, the TEB performance is very stable. There are some minor (~0.1%) orbital variations in the *F* factor, which can be decreased for most bands by refining the weighting scheme of the six BB thermistors used to estimate the BB temperature. In addition, the
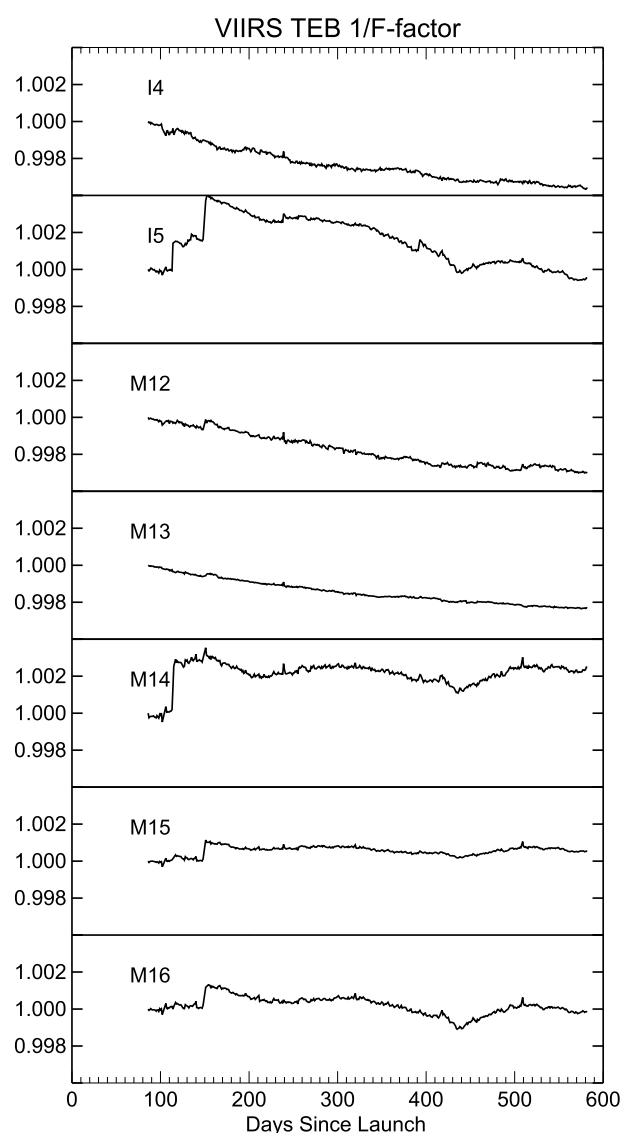
Figure 7. TEB detectors gain (1/*F*) trending from the blackbody calibration. Band averaged *F* factors are computed by the daily average of all detectors and both HAM sides. The trend curve is normalized at day 86 (21 January 2012), the first complete day that the CFPA temperatures stabilized since cyro-cooler door was opened.

calibration coefficients derived during WUCD are in good agreement with those derived from prelaunch calibration and characterization.

The product of the SD BRDF and SAS transmission (RTA view, averaged over all detectors) was derived on orbit from yaw maneuver data as a function of solar declination and azimuth angles. In general, the derived product of the SD BRDF and SAS transmission varies slowly, increasing with lower solar declination and roughly flat with solar azimuth. Figure 8 shows the ratio of the prelaunch measurements to the derived product for band M1 (in agreement to within 1.0%), with the largest differences occurring at high solar declination and low solar azimuth or at low solar declination and high solar azimuth. The differences introduced into the *F* factor could be as high as about ±0.3 % per orbit. Due to the averaging over an orbit, the maximum difference in *F* factor is smaller than the largest difference in transmission factors at a given solar azimuth and declination. The derived product of the SD BRDF and SAS transmission (SDSM view) exhibits a similar shape and the differences between the derived and prelaunch measurements are comparable to those observed for the RTA view.

The computed SDSM screen transmission for SDSM detector 8 is shown in Figure 9 as a function of SDSM azimuth and elevation angles; here the screen transmission was normalized to the highest value. Distinct ridges at roughly constant SDSM elevation angles are visible, and the transmission generally decreases with SDSM azimuth angle. The prelaunch screen transmission did not characterize the distinct ridges in SDSM elevation well due to inadequate angular sampling. In addition, the differences tend to increase with decreasing SDSM azimuth angle for the higher number detectors and the opposite for lower number detectors. The maximum difference among SDSM detectors is as high as 3%. The SDSM detector dependent screen transmission function is used in equation (6) to compute the *H* factor. The variability that existed in the early *H* factor trending, particularly in the higher number detectors, has been diminished through the use of the yaw maneuver-derived transmission functions, although it is not completely corrected. Moreover, the overall trend for the lower number detectors is markedly different, particularly for detector 2. Including nonyaw maneuver data to fill in the gaps in SDSM azimuth may further reduce this variability.

Pitch maneuver data have been successfully used to characterize the TEB RVS. Results shown in Figure 10 are derived from a total of 40 consecutive scans (20 for each HAM side). An average of 20 scans and 10 samples per scan is used for each AOI before the fitting. A further average over all detectors except for the edge
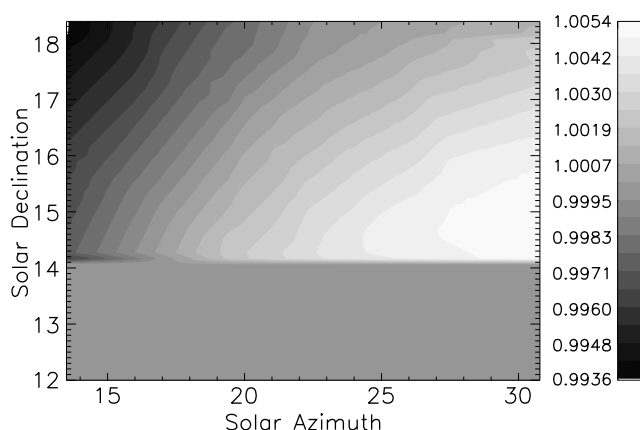
Figure 8. Contour plot of the ratio of the SD transmission factors (the product of the SD BRF and SAS transmission) derived on orbit to the prelaunch measurement as seen by the RTA as a function of solar azimuth and declination angles. The transmission factors shown here are for band M1, averaged over all detectors. Note that for the area in which the solar declination angle is lower than 14°, no prelaunch measurement exists.

detectors affected by the bow-tie deletion is conducted. Typical fitting residuals are found to be within ±0.1%. As shown in Figure 10b, the differences between pitch maneuver and prelaunch RVS are less than 0.3% for all TEB with the exception of M13 with a slightly larger difference of up to 0.5%. Similar agreement between pitch maneuver and prelaunch RVS is found for both HAM sides.

Detector SNR and NEdT are key sensor performance parameters, which are described in the Sensor Specification for VIIRS by Raytheon Company (unpublished document, 2007). On-orbit results of VIIRS SNR for RSB and NEdT for TEB are summarized in Table 1. They are presented using the ratios of on-orbit values to the specifications at the L_{TYP} or T_{TYP}. The RSB SNRs are derived from SD and SV observations. Because of different solar illumination angles, the RSB detectors have different levels of SD responses. The SNRs are computed at all the levels and then fitted as a function of radiance level. Note that the SD screen may cause small nonuniformity in detector responses. However, its impact on RSB F factors and SNRs is extremely small due to corrections applied for the SD screen transmission. The on-orbit values shown in Table 1 correspond to the SNRs at the typical radiance level (L_{TYP}). Ratios larger than 1 indicate that the performance is better than the sensor design requirements. The TEB NEdTs are calculated as a function of temperature during BB WUCD, using BB cool-down data. The resulting NEdT at T_{TYP} shown in Table 1 is better than the sensitivity requirement for all TEB bands (NEdT ratios < 1), and is consistent between all data sets (Columns 9–13), which correspond to a total of 5 on-orbit BB WUCDs performed from launch to 31 May 2013. For comparison purposes, the prelaunch SNR and NEdT values are also presented. As shown in Table 1, the VIIRS was built with large SNR and NEdT performance margins. Consistent with the model prediction [*Lei et al.*, 2012b], the large degradation experienced in the NIR and SWIR bands has gradually leveled off. It is expected that the VIIRS overall performance will continue to meet the sensor design requirements over its 7 year design lifetime. It is clear that a dedicated calibration effort remains the key to the mission success.

The uncertainty of the retrieved RSB top of atmosphere reflectance includes both random and systematic errors. The main source of random error is the EV dn noise, quantified by the SNR at L_{TYP}. The effect of SD dn noise on the F factor uncertainty is reduced to a negligible level through averaging over many samples and scans per orbit. The main
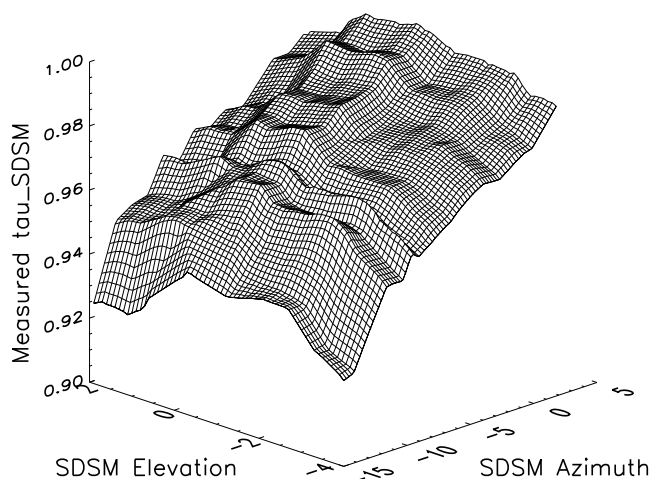

Figure 9. Vignetting function for the SDSM solar transmission screen as a function of SDSM azimuth and elevation angles. The SDSM screen transmission (detector 8 shown here) is normalized to its highest point.
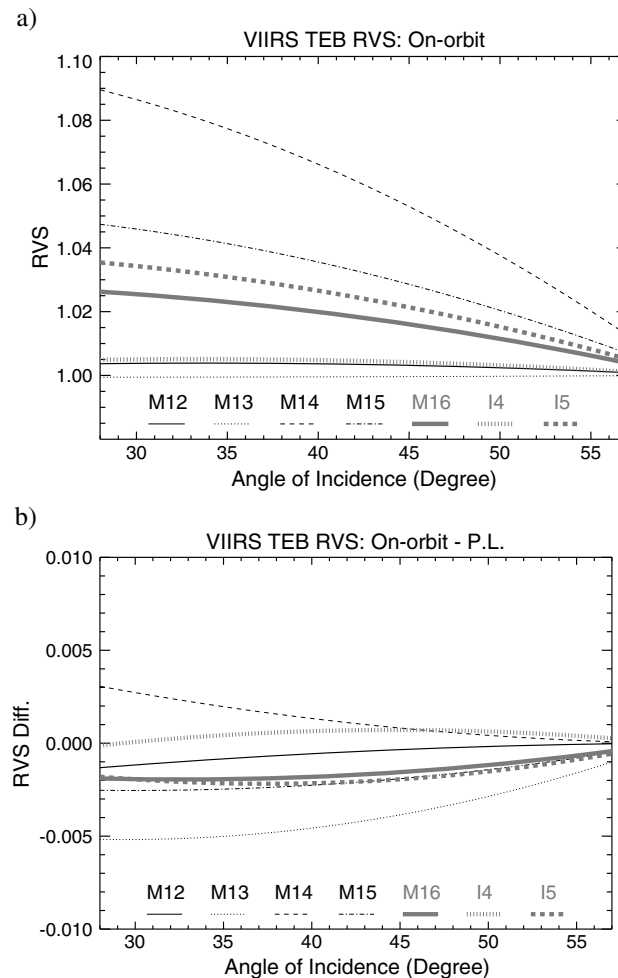
a)

b)

Figure 10. (a) TEB band averaged RVS for HAM side A derived from the pitch maneuver. A second order polynomial is used to compute the RVS as a function of AOI; (b) TEB RVS differences between prelaunch (P.L.) and on-orbit measurements for HAM side A.

contributor to the systematic uncertainty is the SD BRDF prelaunch characterization: 1.09% for the VISNIR bands and 1.32% for the SWIR bands [*Lessel and McClain*, 2007]. The contribution from the *H* factor systematic uncertainties is estimated to be 0.35% [*Fulbright et al.*, 2013]. The systematic uncertainties due to attenuation screen effects are estimated to be 0.25%, while the EV RVS uncertainty effects are estimated to be 0.1% [*Wu et al.*, 2011]. The consequence of any uncertainty in the RSR should be negligible, as the in-band contribution is over 99%. Including all the factors mentioned above, our best estimation of the SDR reflectance uncertainties at L_{TYP} are 1.2% for bands M1–M7, 1.3% for bands I1 and I2, 1.4% for band M10, 1.5% for bands M8 and M9, 1.6% for band I3, and 4.9% for band M11. The relatively large uncertainty for band M11 is due to the very low L_{TYP} value, resulting in a lower SNR value (~20 at present) as compared to other bands. There is an on-going effort to further improve the uncertainty modeling and calculation and the resulting estimates will be published in a future paper.

The uncertainty in the TEB measurements at the SDR product level was assessed by *McIntire et al.* [2013] at different Earth scene temperatures and instrument conditions (scan angles and aggregation modes). The terms dominating the uncertainty for MWIR bands are the BB radiance uncertainty and the EV dn noise. At scenes of 270 K and warmer, the MWIR M bands have an uncertainty on the order of 0.1 K. At lower temperature scenes, this uncertainty increases to about 1 K at 230 K. The LWIR bands uncertainty is dominated by the zeroth order calibration coefficient (the offset) especially at low scene temperatures. The LWIR M bands have 0.15 K to 0.3 K uncertainties for scene temperatures above 230 K. At very low temperatures (about 190 K), the uncertainty reaches about 1 K for M14 and 0.6 K for M15 and M16. The I bands have a higher uncertainty contribution from EV noise compared to M bands at the similar wavelengths, and their uncertainty at 267 K is about 0.5 K and 0.3 K for I4 and I5, respectively.

The VIIRS SDR product uncertainty was not optimal in the months following S-NPP launch. To ensure a better SDR product quality, problems that are found with the instrument or in the SDR production software are monitored by a team of scientists and engineers and documented with detailed reports. Some of the key SDR enhancements already implemented include the following: the update of RSR LUT for the RSB to account for the on-orbit RTA mirror degradation, the corrections of the dual gain band M13 calibration, the implementation of the DNB stray light correction, the updates to SD and SDSM screen LUTs, and many other minor, but substantial, code and LUT fixes. The process of improving the SDR products is ongoing, of course, as VIIRS changes on orbit and as the involved scientists and engineers continue to monitor and characterize the instrument.

5. Summary

S-NPP VIIRS has successfully operated for more than 1.5 years, showing excellent radiometric performance and stability. All OBCs have been operated nominally according to their design and planned calibration activities and continue to provide high quality and timely calibration data used in the SDR operational processing. With on-orbit calibration improvements and updates, the newly generated SDRs are expected to produce high quality EDRs. The RSB calibration uses the SD and SDSM data to generate per orbit gain factors. The TEB calibration is performed on a scan-by-scan basis using the on-board BB. Numerous spacecraft maneuvers were performed at the beginning of the mission to verify and update some key sensor parameters. The yaw maneuver data were used to enhance the SD and SDSM screen transmissions and SD BRDF products. These enhancements have been applied to the operational SDR production. The pitch maneuver data confirmed the good quality of the TEB RVS. Roll maneuvers have been performed on a near-monthly basis for lunar observations to provide an independent verification of the RSB calibration stability determined from on-board SD and SDSM system. The trending of major key parameters, such as the *F* factor, the signal to noise ratio, and temperature, has been performed continuously and has always been within expectations. The large degradation in the NIR and SWIR bands has significantly leveled off and its impact has been assessed and addressed. Despite a few sensor anomalies observed on orbit, the VIIRS overall performance remains excellent.

References

Ardanuy, P., C. F. Schueler, S. W. Miller, P. S. Kealy, S. A. Cota, J. K. Haas, and C. Welsch (2002), NPOESS VIIRS design process, *Proc. SPIE*, *4483*, 22–34.

Barnes, W., X. Xiong, B. Guenther, and V. Salomonson (2003), Development, characterization, and performance of the EOS MODIS sensors, *Proc. SPIE*, *5151*, 337–345.

Barrie, J. D., P. D. Fuqua, M. J. Meshishnek, M. Ciofalo, C. Chu, J. Chaney, R. Moision, and L. Graziani (2012), Root cause determination of on-orbit degradation of the VIIRS rotating telescope assembly, *Proc. SPIE*, *8510*, 851009.

Bruegge, C. J., A. E. Stiegman, R. A. Rainem, and A. W. Springsteen (1993), Use of Spectralon as a diffuse reflectance standard for in-flight calibration of earth-orbiting sensors, *Opt. Eng.*, *32*(4), 805–814.

Butler, J., X. Xiong, A. B. Barnes, F. S Patt, J. Sun, and K. Chiang (2012), An overview of Suomi NPP VIIRS calibration maneuvers, *Proc. SPIE*, *8510*, 85101J.

Cao, C., F. De Luccia, X. Xiong, R. Wolfe, and F. Weng (2013), Early on-orbit performance of the Visible Infrared Imaging Radiometer Suite (VIIRS) onboard the Suomi National Polar-orbiting Partnership (S-NPP) satellite, *IEEE Trans. Geosci. Remote Sens.*, doi:10.1109/TGRS.2013.2247768, in press.

De Luccia, F. J., C. Cao, X. Xiong, R. Wolfe, H. Oudrari, K. Chiang, E. Johnson, S. Mills, L. Liao, D. Moyer, and K. Rausch (2012a), National polar-orbiting partnership (NPP) VIIRS sensor data record (SDR) quality, IEEE Int. Geosci. Remote Sens. Symp., pp. 7189–7192, Munich, Germany.

De Luccia, F. J., D. Moyer, E. H. Johnson, K. W. Rausch, N. Lei, K. Chiang, X. Xiong, E. M. Haas, J. Fulbright, and G. Iona (2012b), Discovery and characterization of on-orbit degradation of the VIIRS rotation telescope assembly, *Proc. SPIE*, *8510*, 85101A.

Fulbright, J., N. Lei, B. Efremova, X. Chen, and X. Xiong (2013), Improving the characterization and performance of the Suomi-NPP VIIRS solar diffuser stability monitor, *Proc. SPIE*, *8866*, 88661J.

Iona, G., E. H. Johnson, M. Ayers, F. De Luccia, L. Graziani, B. Guenther, B. Kennedy, C. J. Kent, R. Lambeck, X. Xiong, and E. Waluschka (2012), VIIRS on-orbit optical anomaly: Lessons learned, *Proc. SPIE*, *8510*, 85101C.

Kieffer, H. H., and T. C. Stone (2005), The spectral irradiance of the Moon, *Astronom. J.*, *129*, 2887–2901.

Lee, T., S. Miller, C. Schueler, and S. Miller (2006), NASA MODIS previews NPOESS VIIRS capabilities, *Weather Forecasting*, *21*(4), 649–655.

Lei, N., Z. Wang, J. Fulbright, S. Lee, J. McIntire, K. Chiang, and X. Xiong (2012a), Initial on-orbit radiometric calibration of the Suomi NPP VIIRS reflective solar bands, *Proc. SPIE*, *8510*, 851018.

Lei, N., Z. Wang, B. Guenther, X. Xiong, and J. Gleason (2012b), Modeling the detector radiometric response gains of the Suomi NPP VIIRS reflective solar bands, *Proc. SPIE*, *8533*, 853319.

Lessel, L., and S. McClain (2007), Low uncertainty measurements of bidirectional reflectance factor on the NPOESS/VIIRS solar diffuser, *Proc. of SPIE*, *6677*, 66771O.

McIntire, J., B. Efremova, D. Moyer, S. Lee, and X. Xiong (2012), Analysis of Suomi-NPP VIIRS vignetting functions based on yaw maneuver data, *Proc. SPIE*, *8510*, 851001K.

McIntire, J., B. Efremova, and X. Xiong (2013), S-NPP VIIRS on-orbit uncertainty estimate for emissive bands, CALCON, Logan, Utah.

Murphy, R. P., P. E. Ardanuy, F. De Luccia, J. E. Clement, and C. Schueler (2006), The visible infrared imaging radiometer suite, in *Earth Science Satellite Remote Sensing*, vol. 1, pp. 199–223, Springer, New York.

Oudrari, H., J. McIntire, D. Moyer, K. Chiang, X. Xiong, and J. Butler (2012), Preliminary assessment of Suomi-NPP VIIRS on-orbit radiometric performance, *Proc. SPIE*, *8510*, 851011.

Salomonson, V., W. Barnes, X. Xiong, S. Kempler, and E. Masuoka (2002), An overview of the Earth Observing System MODIS instrument and associated data systems performance, Proc. IEEE Int. Geosci. Remote Sens. Symp., pp. 1174–1176.

Schueler, C. F., E. Clement, P. Ardanuy, C. Welsh, F. De Luccia, and H. Swenson (2002), NPOESS VIIRS sensor design overview, *Proc. SPIE*, *4483*, 11–23.

Sun, J., X. Xiong, W. L. Barnes, and B. Guenther (2007), MODIS reflective solar bands on-orbit lunar calibration, *IEEE Trans. Geosci. Remote Sens.*, *43*, 2383–2393.

Sun, J., X. Xiong, and J. Butler (2012), NPP VIIRS on-orbit calibration and characterization using the Moon, *Proc. SPIE*, *8510*, 85101I.

Wu, A., J. McIntire, X. Xiong, F. De Luccia, H. Oudrari, D. Moyer, S. Xiong, and C. Pan (2011), Comparison of VIIRS pre-launch RVS performance using results from independent studies, *Proc. SPIE*, *8153*, 81530L.

Wu, A., X. Xiong, K. Chiang, and S. Chengbo (2012), Assessment of the NPP RVS for the thermal emissive bands using the first pitch maneuver observations, *Proc. SPIE, 8510*, 85100P.

Xie, X., X. Xiong, D. Moyer, J. Sun, X. Liu, and W. Barnes (2005), Analysis of MODIS solar diffuser screen vignetting function, *Proc. SPIE, 5882*, 58820T.

Xiong, X., J. Sun, A. Angal, K. Chiang, and W. Barnes (2007a), Applications and results of MODIS lunar observations, *Proc. SPIE, 6744*, 67441H.

Xiong, X., J. Sun, W. Barnes, V. Salomonson, J. Esposito, H. Erives, and B. Guenther (2007b), Multiyear on-orbit calibration and performance of Terra MODIS reflective solar bands, *IEEE Trans. Geosci. Remote Sens., 45*(4), 879–889.

Xiong, X., X. Xie, A. Angal, J. Choi, J. Sun, and W. L. Barnes (2007c), Characterization of MODIS solar diffuser on-orbit degradation, *Proc. SPIE, 6677*, 66770O.

Xiong, X., K. Chiang, J. Sun, W. Barnes, B. Guenther, and V. Salomonson (2008), NASA EOS Terra and Aqua MODIS on-orbit performance, *Adv. Space Res., 43*, 413–422.

Xiong, X., B. N. Wenny, A. Wu, W. Barnes, and V. Salomonson (2009), Aqua MODIS thermal emissive bands on-orbit calibration, characterization, and performance, *IEEE Trans. Geosci. Remote Sens., 47*(3), 803–814.

Xiong, X., J. Sun, X. Xie, W. Barnes, and V. Salomonson (2010), On-orbit calibration and performance of aqua MODIS reflective solar bands, *IEEE Trans. Geosci. Remote Sens., 48*(1), 535–546.

Xiong, X., K. Chiang, J. McIntire, H. Oudrari, A. Wu, M. R. Schwaller, and J. J. Butler (2012), Early assessment of VIIRS on-orbit calibration and support activities, IEEE Int. Geosci. Remote Sens. Symp., pp. 7189–7192, Munich, Germany.